ISSN: 2414-1895 DOI: 10.6919/ICJE.202607_12(7).0015

Failure Mechanism of Airtightness Detection Caused by Corrosion-Induced Clogging in Power Battery Liquid Cooling Plates

Enhan Wen[1], Yan Shi[1,2,*], Wei Shi[3], Yuan Qin[1], Jiayi Gong[1], Anliang Gou[3], Hao Peng[1], Shengtao Yin[1], and Tianxiang Liu[1]

[1] School of Mechanical Engineering, Sichuan University of Science & Engineering, Yibin 644000, China

[2] Sichuan Provincial Engineering Laboratory of Mine Tailings Resource Utilization, Sichuan University of Science & Engineering, Yibin 644000, China

[3] Runthrough Heat Exchange Co. Ltd, Yibin 644000, China

[*]Corresponding Author E-mail: sy71Email@163.com

Abstract

Leakage detection of coolant is critical for the safe operation and maintenance of power battery liquid cooling systems. However, a false-negative phenomenon has frequently been observed in engineering practice: dry-air airtightness tests indicate acceptable sealing performance even though corrosion-induced perforation has already occurred. To reveal the underlying mechanism, a multi-physics coupling model integrating electrochemical corrosion, ionic transport, precipitation kinetics, and porous seepage was developed based on an actual field failure case. Accelerated galvanic corrosion experiments were further conducted to validate the corrosion morphology and failure mode. The results demonstrate that galvanic corrosion between the aluminum liquid cooling plate and the steel battery enclosure leads to the formation of an occluded corrosion cell. Hydrolysis of Al^{3+} ions induces an autocatalytic "dissolution–acidification–accelerated dissolution" cycle, which continuously promotes localized corrosion growth. Meanwhile, Al^{3+} and OH^- ions accumulate near the defect channel and lead to preferential precipitation of $Al(OH)_3$ corrosion products. The local deposition density reaches approximately 1321 kg/m^3 , causing the permeability of the leakage channel to decrease from 10^{-11} m^2 to below 10^{-15} m^2. Consequently, the seepage capacity of the leakage path is essentially lost. To quantitatively evaluate the risk of leakage misdetection, a False-Negative Index (FNI) is proposed. When FNI exceeds 0.99, conventional dry-air airtightness testing becomes incapable of identifying existing leakage defects. Furthermore, three-dimensional airtightness simulations show good agreement with experimental measurements, with pressure-drop deviations below 8%. The proposed mechanism successfully explains the contradiction between actual corrosion perforation and qualified airtightness test results. The findings provide theoretical support for leakage diagnosis, corrosion prevention, and safety-oriented design of battery liquid cooling systems.

Keywords

Liquid Cooling Plate; Galvanic Corrosion; Multi-Physics Simulation; Corrosion Product Deposition; Failure of Airtightness Detection.

ISSN: 2414-1895 DOI: 10.6919/ICJE.202607_12(7).0015

1. Introduction

Coolant leakage is one of the most severe failure modes of power battery liquid cooling systems. It not only causes loss of cooling performance but also leads to insulation degradation, short circuits, and even thermal runaway accidents[1]. Therefore, the reliability of leakage detection is directly related to system safety. At present, dry-air airtightness testing, typically using dry nitrogen or compressed air, is the mainstream inspection method for liquid cooling plates during production and after vehicle assembly. Its underlying assumption is that the existence of any through-wall leakage path will inevitably generate a detectable pressure drop or gas flow signal. However, engineering practice has revealed a contradictory phenomenon: battery packs returned after field failure may still pass dry-air airtightness testing, whereas subsequent disassembly identifies corrosion-induced through perforation in the liquid cooling plate. This false-negative phenomenon has been reported in failure analyses of battery liquid cooling systems[2], yet its underlying mechanism remains insufficiently understood.

Previous studies on failure mechanisms of battery liquid cooling systems have mainly focused on vibration fatigue, mechanical impact, and seal aging[3], while limited attention has been paid to the influence of coolant-leakage-induced galvanic corrosion on leakage detection reliability. Liquid cooling systems commonly adopt aluminum liquid cooling plates integrated with steel battery enclosures. Once leaked coolant accumulates locally, an electrolyte environment is established, facilitating galvanic corrosion. Aluminum acts as the anode and undergoes dissolution, while corrosion products such as $Al(OH)_3$ may continuously deposit within defect channels, progressively altering seepage behavior and obstructing gas penetration during airtightness testing, thereby increasing the risk of false-negative detection. Although existing studies have investigated corrosion behavior and material degradation mechanisms, quantitative understanding of how corrosion product deposition affects seepage evolution and airtightness detection remains limited, restricting the development of effective detection and mitigation strategies.

To address this issue, this study investigates an actual electric vehicle insulation failure case and combines accelerated galvanic corrosion experiments with multi-physics simulation. A coupled model incorporating electrochemical corrosion, ionic transport, precipitation kinetics, and porous seepage is established to reveal the mechanism of corrosion-induced self-blockage and airtightness detection failure. Furthermore, a quantitative relationship between defect-channel permeability decay and detection reliability is developed, and a False Negative Index (FNI) is introduced to evaluate the risk of leakage misdetection. The findings provide theoretical support for leakage diagnosis, corrosion prevention, and safety-oriented design of battery liquid cooling systems.

2. Failure Case and Experimental Verification

2.1 Failure Background

A pure electric vehicle experienced insulation failure in its power battery liquid cooling system after approximately 9,000 km of service. After disassembly of the battery pack cover, accumulated liquid and extensive white corrosion products were observed between the lower battery enclosure and the liquid cooling plate. The liquid cooling plate was made of Al3003 aluminum alloy with a wall thickness of 3 mm. The coolant consisted of 50 vol% ethylene glycol and 50 vol% deionized water[4]. Cell terminals and connectors were mainly copper, while the lower battery enclosure was made of HC420/780DP dual-phase steel[5]. Thermal conductive structural adhesive was applied between the battery modules and the liquid cooling plate.

ISSN: 2414-1895 DOI: 10.6919/ICJE.202607_12(7).0015

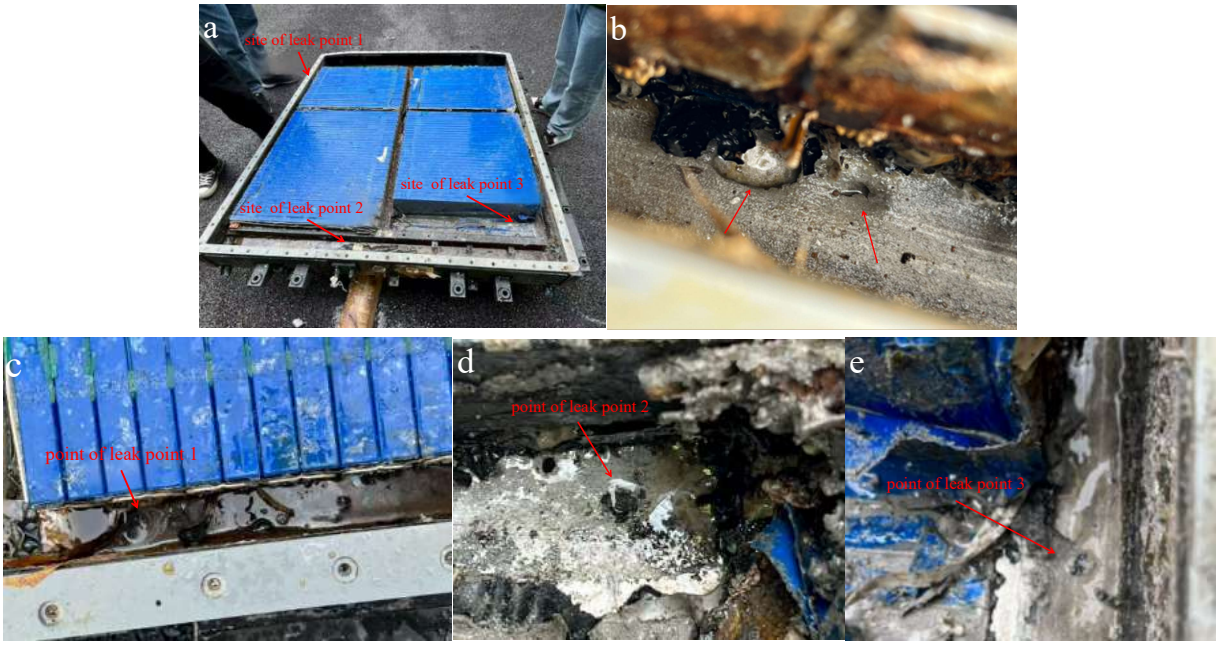

Fig. 1 Disassembly appearance and corrosion morphology of the faulty battery pack (a)Schematic illustration of leakage locations on the liquid cooling plate, (b)Local galvanic corrosion characteristics, (c) Morphology of leak point 1, (d)Morphology of leak point 2, (e)Morphology of leak point 3

2.2 Key Characteristics of the Failure

Systematic failure analysis identified the following key characteristics:

(1) Airtightness tests passed throughout the entire inspection process: all production-stage inspections, battery pack assembly tests, and final vehicle acceptance tests satisfied the enterprise acceptance criteria. After the failed component was returned for investigation, repeated airtightness testing under multiple operating conditions still showed leakage values below the acceptance threshold, even when the test pressure was increased from 250 kPa to 300 kPa. This discrepancy between actual leakage and airtightness test results suggests that the leakage pathway may have been blocked or that the detection sensitivity was insufficient.

(2) Through-corrosion perforation exposed after adhesive removal treatment: after removal of adhesive residues and surface deposits, three evident corrosion pits were identified on the liquid cooling plate surface. These pits were distributed near the right side of the coolant inlet/outlet nozzles and along the module edge region, with diameters ranging from approximately 1 mm to 2 mm.

(3) Typical localized corrosion characteristics: the corrosion pits exhibited a characteristic “narrow opening and wide cavity” morphology, and a large amount of white corrosion products remained inside the pits. Multiple metallic materials, including the aluminum liquid cooling plate, steel enclosure, and copper busbars, coexisted in the affected region, which is consistent with localized galvanic corrosion under dissimilar-metal coupling conditions. Therefore, galvanic corrosion was considered the dominant failure mechanism, whereas mechanical damage and vibration fatigue showed no representative failure features.

2.3 Accelerated Galvanic Corrosion Experiment

To verify the feasibility of the galvanic corrosion failure mode and provide morphological and behavioral references for subsequent mechanism analysis, a 48-h accelerated galvanic corrosion experiment was carried out. It should be noted that this experiment uses accelerated using constant voltage and current to shorten the test period and reproduce the failure morphology; it is not intended for quantitative characterization of the actual in-service corrosion rate. The experimental medium consists of a small amount of the same ethylene glycol coolant mixed with an industrial ester

ISSN: 2414-1895 DOI: 10.6919/ICJE.202607_12(7).0015

debonding agent, used solely to accelerate corrosion features, not representing the actual service environment.

The anode specimen was taken from the same batch of cold plates as the failed part (Al3003, initial thickness 1.2 mm); the cathode specimen was taken from the same batch of HC420/780DP dual-phase steel enclosure. A DC power supply was used with the positive terminal connected to the Al3003 specimen and the negative terminal to the steel specimen. The voltage was set to 40 V, current 1 A, and the test lasted 48 h. After corrosion, a digital camera was used to record macro-morphology changes; then the cross-sectional thickness of the aluminum specimen was measured, and scanning electron microscopy (SEM) was used to observe micro-morphology.

Table 1. Main components of the debonding agent

Component	CAS No.	EC No.	Content (%)
Trichloroethane	25323-89-1	/	3~50
Dimethyl sulfate	77-78-1	201-058-1	0.5~25
Acetone	75-09-2	200-838-9	0.3~15
1,2-Propanediamine	6674-22-2	229-713-7	0.1~10

After 48 h, the solution became pale yellow and turbid, with floating white and yellow-brown corrosion products, closely resembling the morphology of the accumulated liquid observed during disassembly of the failed battery pack. This indicates that the accelerated system can well reproduce the corrosion morphology and product deposition features seen in the failed part. The steel specimen surface showed yellow rust stains, typical iron oxides (FeOOH, Fe2O3). The aluminum specimen exhibited dense pitting and exfoliation, with some areas showing layered peeling. The average thickness of the aluminum specimen decreased from an initial 1.2 mm to 1.02 mm, giving an average corrosion rate of about 3.75×10^{-3} mm/h (calculated based on single-side corrosion depth).

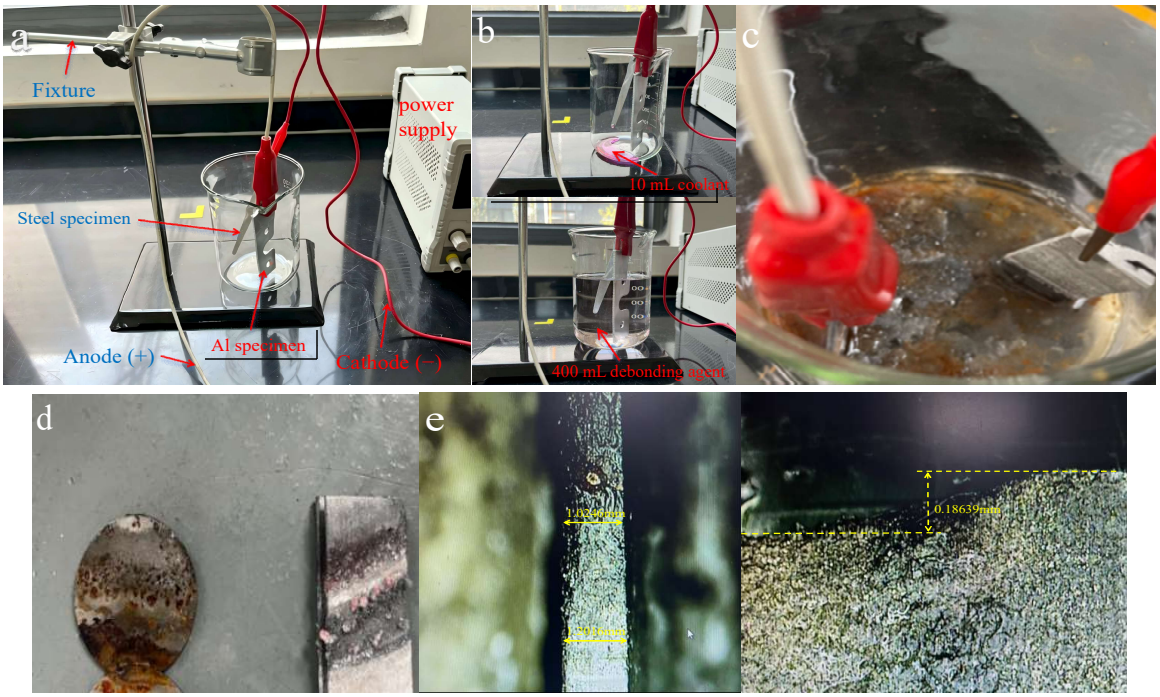

Fig. 2 Accelerated galvanic corrosion experimental setup and results (a)Experimental setup, (b)Electrolyte composition, (c)Solution color change, (d)Surface corrosion of Al and steel specimens, (e)Corrosion depth of Al specimen

ISSN: 2414-1895 DOI: 10.6919/ICJE.202607_12(7).0015

SEM observation showed typical pitting and exfoliation mixed features, with clear pit edges. The "small mouth, large bottom" morphology was consistent with the through-corrosion pits exposed after debonding of the failed part. These results further support the judgment that galvanic corrosion is the dominant failure mechanism, and rule out other failure modes such as mechanical damage. They provide a solid experimental basis for building the failure chain and the simulation model.

2.4 Hypothesized Failure Mechanism

Based on the failure analysis and experimental results, a hypothesized failure chain for the leakage misdetection induced by galvanic corrosion is proposed:

(1) Formation of initial defect: Defect channels introduced during manufacturing or assembly provide an initial channel for coolant leakage. During operation, coolant slowly leaks through these defects and accumulates between the cold plate and enclosure, creating a persistent electrolyte that enables galvanic corrosion[6,7].

(2) Galvanic corrosion initiation: The aluminum cold plate and steel enclosure form a galvanic couple, with aluminum being the anode due to its lower potential[8,9]. Cl^- ions preferentially adsorb at defects of the passive film, destroying it and inducing pitting.

(3) Localized acceleration and autocatalytic dissolution cycle: The geometric singularity of the defect edge causes a high current density concentration, which together with the different characteristic dimensions of the anode and cathode further accelerates local corrosion. As the pit develops, its interior becomes an occluded cell with limited oxygen diffusion. Aluminum continues to dissolve anodically; hydrolysis of Al^{3+} releases H^+, lowering pit pH and forming an autocatalytic 'dissolution–acidification–accelerated dissolution' cycle that drives pit growth[10,11].

(4) Through-wall perforation and blockage by corrosion products: As corrosion progresses, the cold plate eventually undergoes through-wall corrosion, and coolant leaks through the perforation, causing an insulation failure. Meanwhile, $Al(OH)_3$ deposits in the defect channel, gradually reducing its permeability. During factory dry-air airtightness testing, the test gas is unable to pass through the partially blocked micro-channel, resulting in a false-negative "pass" result despite the actual existence of a through-perforation.

(5) Exposure of perforation after debonding treatment: Immersion in industrial ester debonding agent removes corrosion products and residual adhesive, exposing the perforation and confirming through-corrosion damage The entire corrosion failure and dynamic blockage process is illustrated in Fig. 3.

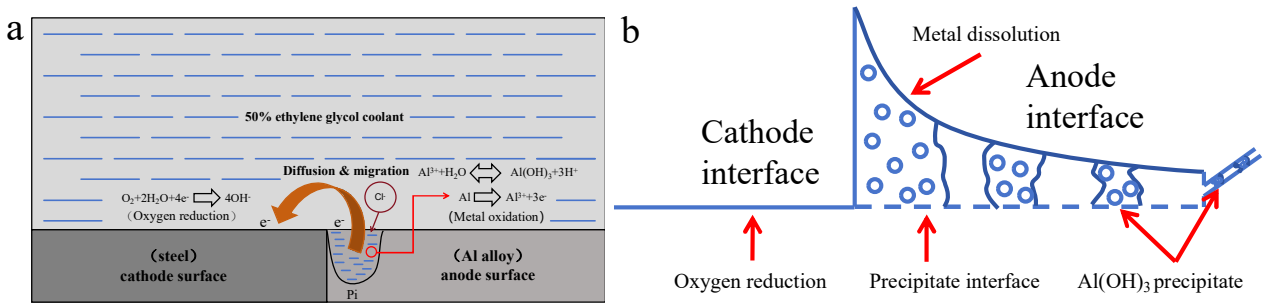

Fig. 3 Mechanism of corrosion failure and dynamic blockage by precipitates (a)Corrosion mechanism, (b)Blockage mechanism

3. Multi-physics Simulation Model and Experimental Methods

3.1 Basic Governing Equations

To quantitatively analyze the blockage of leakage channels and the misjudgment mechanism induced by corrosion product deposition, a multi-physics model coupling electrochemical reactions, ionic mass transfer, precipitation kinetics, and porous media flow is developed. The governing equations

ISSN: 2414-1895 DOI: 10.6919/ICJE.202607_12(7).0015

are given below (where ∇ is the gradient operator, $\nabla\cdot$ is the divergence operator, and ∇^2 is the Laplace operator).

3.1.1 Galvanic Corrosion Kinetics

A secondary current distribution interface is used to describe the galvanic corrosion process. Under a quasi-steady-state assumption, charge conservation holds in the electrolyte domain, as expressed in Eq. (1):

$$\nabla\cdot\left(\sigma_e\nabla\phi_l\right)=0 \tag{1}$$

where σ_e is the electrolyte conductivity (S/m) and ϕ_l is the electrolyte potential (V). The electrochemical reaction at the electrode surface is driven by the overpotential, i.e., the difference between the electrode potential ϕ_s (V, metal phase potential) and ϕ_l.

The electrode kinetics are described by the Butler–Volmer equation. The anodic (Al3003) aluminum dissolution reaction is given by Eq. (2):

$$i_{loc\_an}=i_{o\_an}\cdot 10^{\frac{\left(\phi_s-\phi_l-E_{eq\_an}\right)}{A_{an}}} \tag{2}$$

The cathodic (HC420/780DP dual-phase steel) oxygen reduction reaction[12] is given by Eq. (3):

$$i_{loc\_cat}=-i_{o\_cat}\cdot 10^{\frac{\left(\phi_s-\phi_l-E_{eq\_cat}\right)}{A_{cat}}} \tag{3}$$

where i_{0_an} and i_{0_cat} are the anodic and cathodic exchange current densities (A/m^2), E_{eq_an} and E_{eq_cat} are the equilibrium potentials (V), A_{an} and A_{cat} are the anodic and cathodic Tafel slopes (V), and ϕ_s is the electrode potential (V, metal phase potential).

The corrosion removal rate at the anode interface is calculated by Faraday's law and serves as a boundary condition for the arbitrary Lagrangian–Eulerian (ALE) moving mesh to realize dynamic evolution of the corrosion morphology[13,14], as shown in Eq. (4):

$$v_n=\frac{i_{loc\_an}\cdot M_{Al}}{n\cdot F\cdot\rho_{Al}} \tag{4}$$

where v_n is the normal corrosion rate (m/s), M_{Al} is the molar mass of aluminum (kg/mol), n is the number of electrons transferred in aluminum dissolution, F is the Faraday constant (C/mol), and ρ_{Al} is the density of aluminum (kg/m^3).

3.1.2 Ionic Mass Transfer and Precipitation Kinetics

The convective–diffusive–migration behavior of Al^{3+} and OH^- in the electrolyte is described by the Nernst–Planck equation. The electrolyte is considered stagnant, and thus the convection term is neglected, giving Eq. (5):

ISSN: 2414-1895 DOI: 10.6919/ICJE.202607_12(7).0015

$$\frac{\partial c_i}{\partial t} + u \cdot \nabla c_i = D_i \nabla^2 c_i + R_i \tag{5}$$

where c_i is the concentration of ion i (mol/m^3), D_i is the diffusion coefficient (m^2/s), R_i is the reaction source term (mol/(m^3·s)), t is time (s), and u is the ionic mobility. Given that the electrolyte is stagnant, the convection term $u \cdot \nabla c_i = 0$. The generation rate of Al^{3+} is determined by the anodic reaction, and that of OH^- by the cathodic reaction.

The precipitation rate of $Al(OH)_3$ is based on the supersaturation of the ion product relative to the solubility product, using a max function to enforce physical constraints:

$$R_{precip} = K_{precip} \cdot \max\left(\frac{c_{Al} \cdot c_{OH}^3}{K_{sp\_AlOH_3}} - 1, 0\right) \tag{6}$$

where R_{precip} is the precipitation rate (mol/(m^3·s)), K_{precip} is the precipitation rate constant (mol/(m^3·s)), $K_{sp\_Al(OH)_3}$ is the solubility product of $Al(OH)_3$ (mol^4/m^{12}), and c_{Al} , c_{OH} are the concentrations (mol/m^3).

3.1.3 Porous Seepage and Blockage Effect

A modified Kozeny–Carman relationship is used to describe the evolution of porosity and permeability due to precipitate accumulation:

$$\varepsilon = \max\left(\varepsilon_{\min}, \varepsilon_0 \cdot \left(1 - \frac{M_{precip}}{\rho_{precip} \cdot \phi_{\max} \cdot V}\right)\right) \tag{7}$$

$$k = \max\left(k_{\min}, k_0 \cdot \left(\frac{\varepsilon}{\varepsilon_0}\right)^n \cdot \frac{(1-\varepsilon_0)^2}{(1-\varepsilon)^2}\right) \tag{8}$$

where ε is the current porosity, ε_0 the initial porosity, $\varepsilon_{\min}$ the minimum porosity, M_{precip} the mass of precipitated $Al(OH)_3$ (kg), ρ_{precip} the precipitate density (kg/m^3), $\phi_{\max}$ the maximum volume fraction of precipitate, V the control volume (m^3), k the current permeability (m^2), k_0 the initial permeability (m^2), $k_{\min}$ the minimum permeability (m^2)and n the empirical exponent.

After the defect channel is gradually filled with precipitates, it is treated as a porous medium, and gas flow is described by Darcy's law:

$$u = -\frac{k}{\mu}\nabla p, \ \nabla \cdot u = 0 \tag{9}$$

where u is the velocity vector (m/s), μ is the dynamic viscosity (Pa·s), and p is the pressure field (Pa).

3.1.4 False-Negative Index (FNI)

To quantitatively evaluate the impact of corrosion product deposition on the reliability of airtightness testing, a False-Negative Index (FNI) is defined as:

ISSN: 2414-1895 DOI: 10.6919/ICJE.202607_12(7).0015

$$FNI = 1 - \frac{k}{k_0} \tag{10}$$

where k is the current permeability (m^2) and k_0 is the initial permeability (m^2). FNI ranges from 0 to 1; higher values indicate more severe blockage and higher risk of missed detection.

Based on simulation results and typical industrial airtightness testing conditions (test pressure 250–300 kPa, dwell time 60 s), the following risk levels are proposed:

◆ FNI < 0.90: The defect channel remains highly permeable; leakage can be effectively detected by conventional dry-air testing.

◆ 0.90 ≤ FNI < 0.99: Partial blockage occurs, the pressure drop signal is significantly weakened, and a certain risk of missed detection exists.

◆ FNI ≥ 0.99: The defect channel permeability has dropped to about 10^{-15} m^2 , and the pressure drop signal is below the enterprise detection threshold, indicating a high-risk false-negative state.

This index establishes a direct quantitative relationship between the degree of corrosion product deposition and detection reliability, providing a criterion for optimizing engineering testing methods.

3.2 Geometric Model and Boundary Conditions

3.2.1 Two-dimensional Geometric Model

A two-dimensional (2D) cross-sectional model is constructed based on the failed part. It includes the Al3003 cold plate (anode domain, thickness 3 mm), the internal coolant channel, the HC420/780DP steel enclosure (cathode domain) on the left, and a 1.5 mm gap representing the electrolyte accumulation cavity between the enclosure and the cold plate. An initial micro-defect (depth 1.5 mm, diameter 20 μm) is introduced at the cavity–cold plate interface to represent a manufacturing/assembly defect. The bottom protective cover is treated as an external constraint and is not directly involved in electrochemical reactions, thus omitted in the simulation.

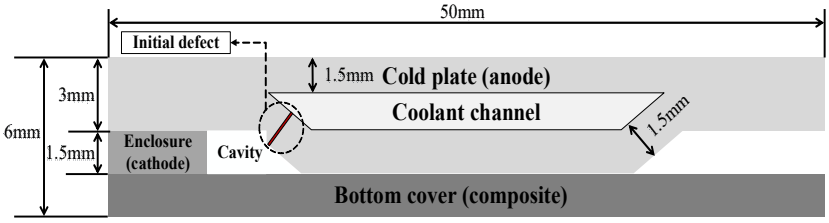

Fig. 4 Two-Dimensional (2D) Cross-Sectional Model

3.2.2 Three-dimensional Fluid Domain Model for Airtightness Testing

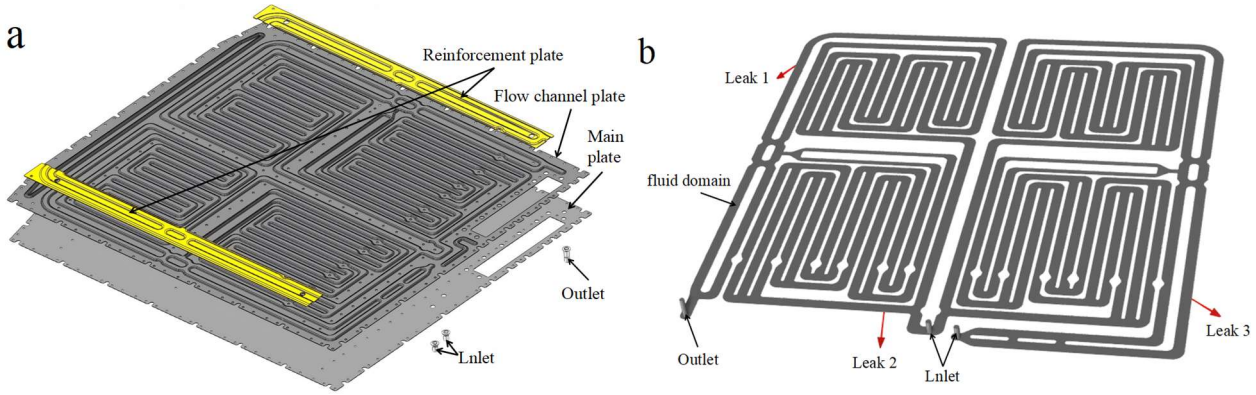

Fig. 5 Schematic of Liquid Cooling Plate Structure and Components (a)schematic of liquid cooling plate structure, (b)schematic of three-dimensional fluid domain

ISSN: 2414-1895 DOI: 10.6919/ICJE.202607_12(7).0015

To reproduce the factory dry-air airtightness test, a full-scale 3D model of the cold plate is built, with flow channels identical to the actual product. The three perforation positions determined from the failed battery pack are set as leakage holes with an equivalent diameter of 20 μm to represent partial blockage by corrosion products. All other boundaries are closed. Initial pressures of 250 kPa and 300 kPa are applied inside the flow channel, while the external boundary is set to 0 Pa gauge pressure (atmospheric), simulating the actual test conditions.

3.3 Key Model Parameters

Electrochemical kinetic parameters are adopted from literature reports of polarization curve fitting results for Al3003 and low-alloy steel in ethylene glycol–water systems; mass transfer and porous media parameters are adopted from relevant studies and calibrated for this operating condition[14–21].

Table 2. Electrochemical kinetic parameters

Parameter	Symbol	Value	Unit
Anodic exchange current density	i_{0_an}	1.0×10^{-4}	A/m^2
Cathodic exchange current density	i_{0_cat}	1.0×10^{-5}	A/m^2
Anodic equilibrium potential	E_{eq_an}	-1.66	V
Cathodic equilibrium potential	E_{eq_cat}	0.20	V
Anodic Tafel slope	A_{an}	0.05	V
Cathodic Tafel slope	A_{cat}	-0.12	V
Electrolyte conductivity	σ	0.15	S/m
Density of aluminum	ρ_{Al}	2700	Kg/m^3

Table 3. Mass Transfer and Porous Media Parameters

Parameter	Symbol	Value	Unit
Al^{3+} diffusion coefficient	D_{Al}	1.0×10^{-9}	m^2/s
OH^- diffusion coefficient	D_{OH}	2.0×10^{-8}	m^2/s
Initial pH	pH_0	7.5	-
$Al(OH)_3$ solubility product	K_{sp}	1.0×10^{-33}	mol^4/m^{12}
Precipitation rate constant	K_{precip}	1.0×10^{-4}	$mol/(m^3\cdot s)$
Precipitate density	ρ_{precip}	2400	Kg/m^3
Initial porosity	ε_0	0.99	-
Minimum porosity	$\varepsilon_{\min}$	0.01	-
Initial permeability	k_0	1×10^{-11}	m^2
Minimum permeability	$k_{\min}$	1.0×10^{-15}	m^2
Empirical exponent	n	3	-

ISSN: 2414-1895 DOI: 10.6919/ICJE.202607_12(7).0015

4. Full-process Simulation Analysis of Corrosion Failure

4.1 Corrosion Initiation and Local Acceleration Mechanism

In the early stage, the current density is highly concentrated at the sharp edge of the cavity on the left side, exhibiting a typical “edge effect”. The geometric singularity of the defect causes local electric field concentration, with equipotential lines converging at the tip, resulting in a large local current density. The anodic interface exposed to the electrolyte is much larger than the cathodic interface (length ratio ≈ 6:1), further concentrating the corrosion current at the defect edge. The combination of edge geometry and area ratio makes corrosion initiate preferentially at the defect edge and creates local acceleration[22]. As shown in Fig. 6, the subsequent pit expansion region is in good agreement with the initial high-current-density region, and the corrosion front generally propagates along the current outflow direction, indicating that local current density dominates the evolution of corrosion morphology.

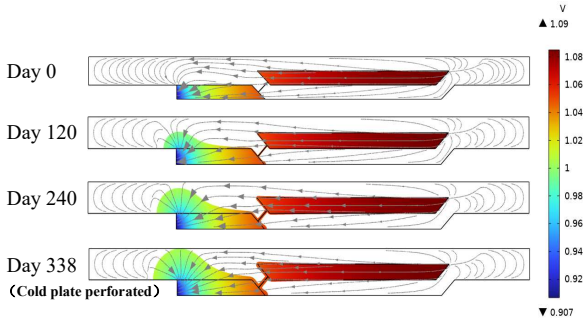

Fig. 6 Distribution of electrolyte potential and vector diagram of current density during corrosion

4.2 Pit Morphology Evolution

Compared with the initial stage, a nearly hemispherical pit appears on the anodic dissolution surface on day 120; by day 240 the pit deepens significantly and approaches perforation; on day 338 the corrosion depth reaches 3 mm, and the cold plate is perforated.

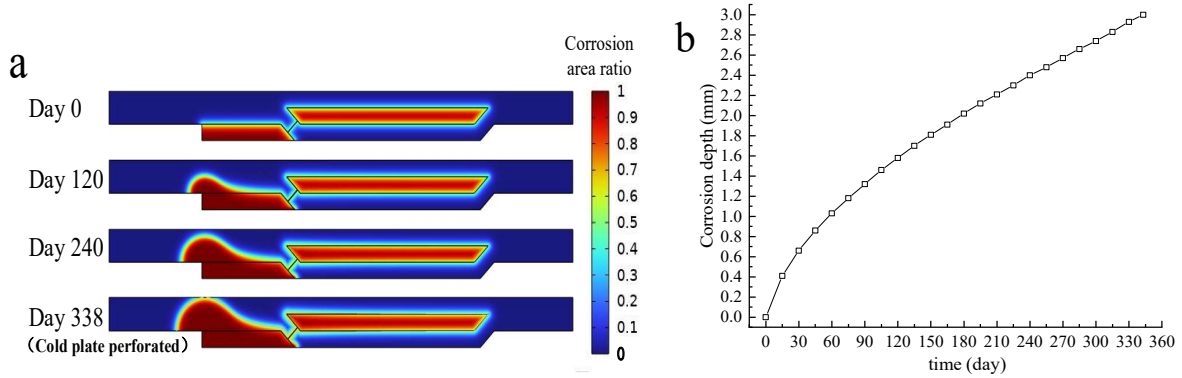

Fig. 7 Evolution of galvanic corrosion area and depth (a)Contour map of dynamic expansion of galvanic corrosion area, (b)Evolution curve of corrosion depth over time

As shown in Fig. 7(b), the corrosion depth increases rapidly in the early stage and then slows down. The high initial corrosion rate is driven by the autocatalytic effect of the occluded cell. Later, partial deposition of corrosion products partially blocks the channel, causing the reaction to become mass-transfer limited. The simulated perforation time is 338 days, indicating that the cold plate is susceptible to through-wall corrosion during long-term service. The result is consistent with the fact that the failed part had already experienced perforation, preliminarily validating the model.

ISSN: 2414-1895 DOI: 10.6919/ICJE.202607_12(7).0015

The perforation time estimated from the 48-h accelerated experiment (33 days) differs by an order of magnitude from the simulation (338 days) because the experiment applies an external current to intensify corrosion, whereas the simulation uses electrochemical parameters representative of actual service conditions. The accelerated experiment serves to verify corrosion morphology and failure mode, while the simulation analyzes corrosion evolution and its effect on airtightness detection under real operating conditions.

4.3 Pit Morphology Evolution

As the pit expands, an occluded microenvironment gradually forms inside, relatively enclosed from the external electrolyte. As seen in Fig. 8, Al^{3+} is mainly concentrated inside the pit, with a peak concentration of 1.23×10^{-6} mol/m^3 ; OH^- is mainly distributed near the cathode region, with a peak concentration of 3.82×10^{-6} mol/m^3 and a gradient. This distribution shows limited mass exchange between pit interior and exterior, reflecting the development of the occluded cell effect.

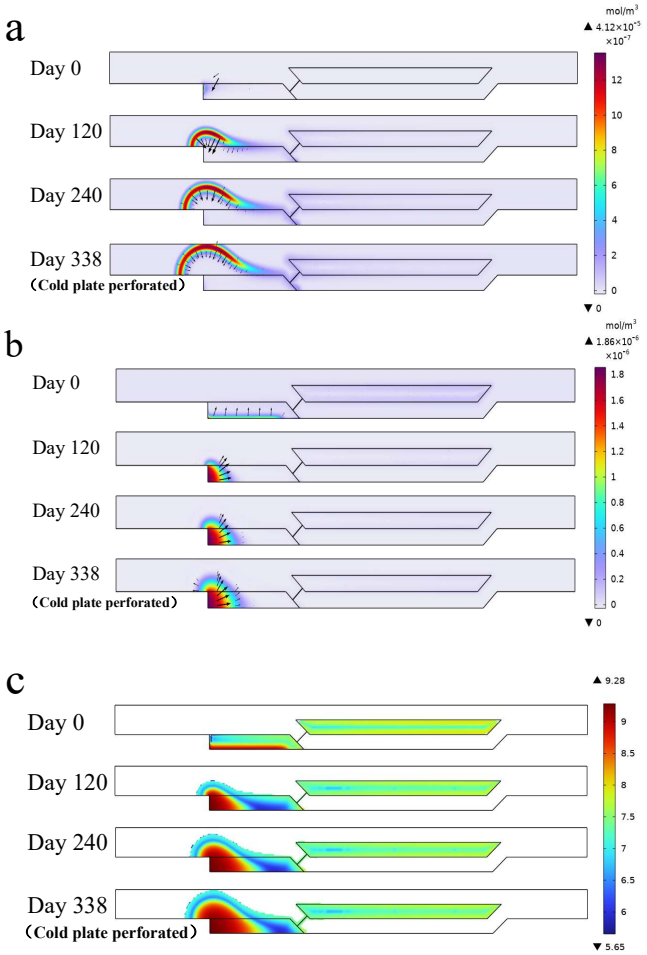

Fig.8 Distribution of ion concentration and pH during corrosion (a)Contour plot of Al^{3+} concentration distribution and ionic flux vector field, (b)Contour plot of OH^- concentration distribution and ionic flux vector field, (c)Contour plot of pH distribution

Crucially, the hydrolysis reaction of Al^{3+} inside the pit:

$$Al^{3+} + 3H_2O \rightarrow Al(OH)_3 \downarrow + 3H^+$$

ISSN: 2414-1895 DOI: 10.6919/ICJE.202607_12(7).0015

continuously releases H^+, causing the the pH at the corrosion front drops from 7.5 to about 6.5, creating a locally acidic environment. This local acidic environment further promotes active dissolution of the aluminum matrix, sustaining the generation of Al^{3+} and forming an autocatalytic "dissolution–acidification–accelerated dissolution" cycle[18], providing the kinetic conditions for continued pit growth. Meanwhile, the continuous exfoliation morphology observed in the accelerated corrosion experiment aligns with this mechanism, supporting the key role of the autocatalytic cycle in corrosion evolution.

4.4 Self-blockage Effect of Corrosion Products

Deposition of $Al(OH)_3$ mainly occurs in three regions: the Al^{3+}-rich zone inside the pit and above the pit mouth, the OH^--rich regions on the cathode side, and the upper-right region extending into the initial defect channel. Although the initial defect area is small, it serves as the only leakage pathway for coolant; accumulation of precipitates in this region directly blocks the flow channel.

As shown in Fig. 9(b), the local accumulation density of precipitates in the defect channel increases nonlinearly with time, being rapid at first and then gradually slowing. In the early stage, autocatalytic dissolution continuously supplies Al^{3+}, leading to rapid precipitation and a fast increase in density. As precipitates progressively fill the pore space, ion transport becomes increasingly restricted, and the precipitation rate decreases. Finally, the local accumulation density reaches about 1321 kg/m^3. Continuous deposition occupies the pore space in the defect channel, reducing permeability from 10^{-11} m^2 to below 10^{-15} m^2 (more than four orders of magnitude) and porosity from 0.99 to 0.096, indicating a severe loss of seepage capacity.

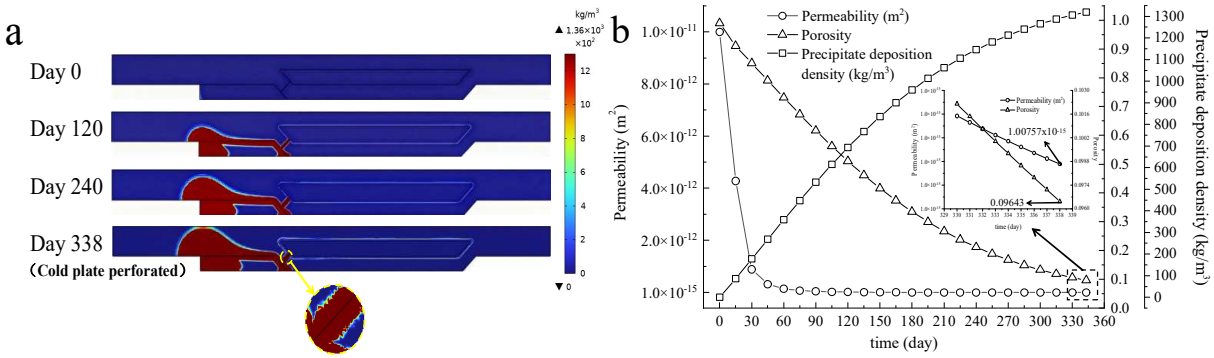

Fig. 9 Deposition distribution of corrosion product $Al(OH)_3$ (a)Contour plot of precipitate distribution, (b)Evolution curves of defect channel parameters

According to the defined FNI, when the permeability drops to 10^{-15} m^2, FNI reaches 0.9999, far exceeding the high-risk threshold of 0.99. At this stage, although a through-defect still exists, the test gas cannot pass through the micro-channel filled with corrosion products under conventional dwell time, causing the pressure-drop signal to fall below the detection threshold and resulting in a missed detection. This quantitatively explains the contradictory phenomenon in which the failed component "had already developed through-wall corrosion but still passed the returned-factory airtightness test".

4.5 3D Airtightness Test Pressure-drop Simulation and Model Validation

Based on the three perforation positions and sizes identified from the failed pack (approx. 20 μm equivalent diameter after partial blockage), a 1:1 3D model was built to simulate the returned-factory dry-air airtightness test. Initial pressures of 250 kPa and 300 kPa were applied, with a dwell time of 60s, external pressure set to 0 Pa gauge, and other boundaries closed.

ISSN: 2414-1895 DOI: 10.6919/ICJE.202607_12(7).0015

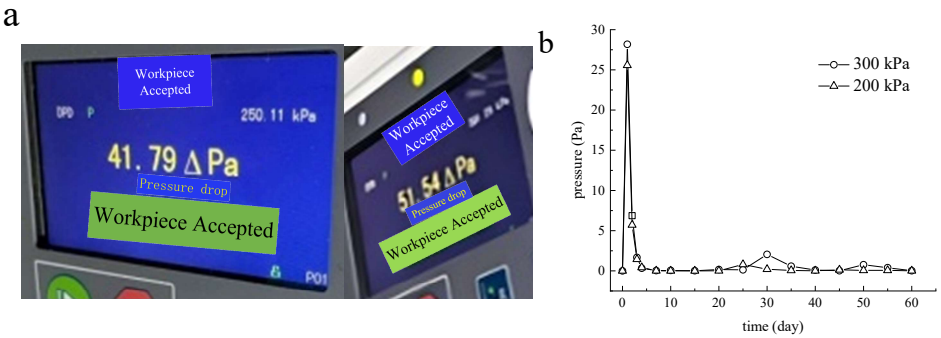

Fig. 10 Airtightness test results (a)Measured data from the pressure holding test, (b)Simulated total pressure drop versus time

The measured results for the returned failed part are shown in Fig.10: at 250 kPa, leakage remained below the detection limit and was judged as "pass"; the same was true at 300 kPa.

The simulation shows total pressure drops of 38.56 Pa at 250 kPa and 54.78 Pa at 300 kPa after 60 s. Relative errors compared to measured values (41.79 Pa at 250 kPa, 51.54 Pa at 300 kPa) are 6.29% and 7.73%, respectively. Good agreement under both conditions indicates that the 3D model accurately reproduces the returned-factory detection process.

Table 4. Comparison between simulation results of the airtightness and measured data

Test condition	Measured value (Pa)	Simulated result (Pa)	Relative error (%)
250 kPa air pressure	41.79	38.56	6.29
300 kPa air pressure	51.54	54.78	7.73

4.6 Summary of Mechanism and Discussion of Protection Strategies

Based on the full-chain failure mechanism revealed above, the following tiered protection and detection improvement strategies are proposed for each key link of the failure chain:

(1) Source prevention of galvanic corrosion: Optimize drainage design at the cold plate–enclosure interface to avoid long-term liquid accumulation; introduce insulating layers at dissimilar-metal contacts to interrupt galvanic corrosion[3].

(2) Process inhibition of corrosion acceleration: Control concentrations of aggressive ions (e.g., Cl−) and add corrosion inhibitors to the coolant; improve stamping and welding processes to reduce initial micro-defects and stress concentration areas[6,7].

(3) Detection-end solution for false-negative airtightness tests: Supplement conventional dry-air testing with wet-condition auxiliary tests or periodic retesting to restore detectability of partially blocked channels; integrate online monitoring of coolant conductivity to provide early warning of abnormal corrosion[18].

5. Conclusion

(1) Based on failed part analysis and simulation, a complete failure chain is proposed: micro-defects lead to coolant accumulation, forming a galvanic environment; this induces corrosion product deposition, resulting in permeability decay and ultimately false-negative airtightness results. Current density concentration at the defect edge, together with the anode–cathode area ratio difference, is the main driving force for corrosion initiation.

(2) Accelerated galvanic corrosion experiments show that the average aluminum specimen thickness decreased from its initial 1.2 mm to 1.02 mm, with an average corrosion rate of 3.75×10^{-3} mm/h. The corrosion morphology is consistent with the failed part, verifying galvanic corrosion as the dominant failure mode.

ISSN: 2414-1895 DOI: 10.6919/ICJE.202607_12(7).0015

(3) Simulation results quantitatively reveal the relationship between corrosion product deposition and permeability decay. Al^{3+} hydrolysis inside pits reduces the local pH from 7.5 to 6.5, forming an autocatalytic cycle. Deposition of $Al(OH)_3$ in the defect channel (self-blocking effect) reduces permeability from 10^{-11} m^2 to 10^{-15} m^2 and porosity to 0.096. The False-Negative Index (FNI) establishes a quantitative link between permeability decay and detection reliability; when FNI ≥ 0.99, conventional dry-air airtightness tests have a significant risk of missed detection.

(4) 3D airtightness test simulations agree well with measurements (total pressure drop error < 8% for 60 s dwell time), validating the model's predictive capability for actual detection processes.

(5) Based on the failure mechanism, protection strategies are proposed, including drainage optimization, dissimilar-metal insulation, wet-condition auxiliary testing, and coolant conductivity monitoring, providing guidance for leakage prevention in battery liquid cooling systems.

Acknowledgments

This work was supported by the project of 2025 Science and Technology Program of Yibin City (2025GY005) for "Key Technology Research and Application of High-Frequency Welding for New Energy Vehicle PACK Cooling Plates", and the 2024 Major Science and Technology Program of Yibin City (2024ZD001) for "Key Technology Research and Application of Intelligent Koji-Making and Fermentation System for Medium and Large-Scale Baijiu Brewing".

References

[1] Yong, T., Wei, Z., Shubin, Y., Xuepeng, Y., Wei, Y., & Shiwei, Z. (2025). Review on phase change heat transfer based high efficiency composite thermal control technology for power battery. Journal of Mechanical Engineering, 61(4), 176–194.

[2] Li, C., Fan, X. R., & Zhou, L. G. (2023). Analysis of liquid leakage problem of power battery water cooling plate. Auto Master, (08), 21–25.

[3] Orangi, S., Manjong, N., Clos, D. P., et al. (2024). Historical and prospective lithium-ion battery cost trajectories from a bottom-up production modeling perspective. Journal of Energy Storage, 76, 109800.

[4] Bashkirtseva, N. Y., Sladovskaya, O. Y., Ovchinnikova, Y. S., et al. (2017). Corrosion inhibitors for water–glycol based cooling systems. Chemistry and Technology of Fuels and Oils, 52(6), 751–755.

[5] Hengchao, G. (2024). Processing technology of a new energy battery roll formed enclosure (Chinese Patent Application No. CN118544067A). China National Intellectual Property Administration.

[6] Dongdong, Z., Cheng, W., Jiyu, Q., et al. (2021). Effect of trace Cl-and Cu^{2+} ions on corrosion behavior of 3A21 Al-alloy in ethylene glycol coolant. Journal of Chinese Society for Corrosion and Protection, 41(3), 383–388.

[7] Chen, X., Tian, W., Li, S., et al. (2016). Effect of temperature on corrosion behavior of 3003 aluminum alloy in ethylene glycol–water solution. Chinese Journal of Aeronautics, 29(4), 1142–1150.

[8] Simin, C., Longjiang, L., Yansong, H., et al. (2025). Galvanic corrosion behavior and reaction mechanism of Cu-Al couple in ethylene glycol-water coolant. Journal of Chinese Society for Corrosion and Protection, 46(1), 299–307.

[9] Shi, L., Yang, X., Song, Y., et al. (2019). Effect of corrosive media on galvanic corrosion of complicated tri-metallic couples of 2024 Al alloy/Q235 mild steel/304 stainless steel. Journal of Materials Science & Technology, 35(9), 1886–1893.

[10] Yin, L., Li, W., Wang, Y., et al. (2019). Numerical simulation of micro-galvanic corrosion of Al alloys: Effect of density of $Al(OH)_3$ precipitate. Electrochimica Acta, 324, 134847.

[11] Håkansson, E., Hoffman, J., Predecki, P., et al. (2017). The role of corrosion product deposition in galvanic corrosion of aluminum/carbon systems. Corrosion Science, 114, 10–16.

[12] Hu, G., Yang, J., & Zheng, X. (2017). Corrosion behavior of aluminum cold plate in ethylene glycol coolant. Corrosion and Protection, 38(11).

[13] Cheng, Y. L., & Zhang, Z. (2009). Comparison of corrosion behaviors of AZ31, AZ91, AM60 and ZK60 magnesium alloys. Transactions of Nonferrous Metals Society of China, 19(3), 517–524.

ISSN: 2414-1895 DOI: 10.6919/ICJE.202607_12(7).0015

[14] Pongsaksawad, W., He, J., Li, C., et al. (2023). Atmospheric corrosion behaviors of 6000-series aluminum alloy under tropical climate influences of Thailand. Materials Testing, 65(6), 924–933.

[15] Johansson, M. V., Testa, F., Zaier, I., et al. (2018). Mass flow rate and permeability measurements in microporous media. Vacuum, 158, 75–85.

[16] Liu, Y., & Cheng, Y. F. (2010). Effects of coolant chemistry on corrosion of 3003 aluminum alloy in automotive cooling system. Materials and Corrosion, 61(7), 574–579.

[17] Miao, H., Yu, H., Wang, H., et al. (2025). Corrosion behavior of 7A09 aluminum alloy exposed to propylene glycol coolant at different conditions. International Journal of Electrochemical Science, 20(9), 101105.

[18] Zuo, H., Fan, J., Liu, F., et al. (2021). Corrosion behavior of 3A21 aluminum alloy in water-ethylene glycol coolant under simulated engine working conditions. International Journal of Electrochemical Science, 16(6), 21062.

[19] Zhu, H. X., He, Z. Y., Jin, G. F., et al. (2023). Review of research methods on galvanic corrosion of aluminum alloy. Surface Technology, 52(2), 135–147, 195.

[20] Haroooni, A., Eskandari, H., Maddahy, M. H., et al. (2015). Corrosion behavior of 6063 aluminum alloy in ethylene glycol-water solution. Iranian Journal of Materials Science & Engineering, 12(4).

[21] Zhao, Q., Zhao, J., Cheng, X., et al. (2020). Galvanic corrosion of the anodized 7050 aluminum alloy coupled with the low hydrogen embrittlement CdTi plated 300M steel in an industrial-marine atmospheric environment. Surface and Coatings Technology, 382, 125171.

[22] Dai, K. H., Sun, Y. W., Chen, Y., & Hou, E. H. (2024). Galvanic corrosion of titanium and aluminum couplings in simulated marine atmospheric environment. Surface Technology, 53(9), 11–21.